

RESEARCH ARTICLE

Count-rate, linearity, and performance of new backgammon detector technology

Hamish A. Melia | Jonathan W. Dean | Lucas F. Smale | Alexis J. Illig |
Christopher T. Chantler 

School of Physics, The University of
Melbourne, Melbourne, Victoria, Australia

Correspondence

Christopher T. Chantler, School of
Physics, The University of Melbourne,
Melbourne, Victoria, Australia.
Email: chantler@unimelb.edu.au

The meander wire backgammon technology has high levels of flux and spatial linearity across a wide range of energies. One of the attractive features of these technologies is the stability of response and robustness under long X-ray exposure, compactness, and portability. A key problem historically has been the limited range of count-rate for processing to the optimum resolution. We report dramatic advances in this and other areas appropriate for high-accuracy experiments including tests of quantum electrodynamics, fundamental relativistic atomic physics, X-ray calibration, and crystallography. We illustrate this technology applied to the $K\alpha_{1,2}$ spectra of titanium, chromium, and copper. The quality of the spectra permits deeper insight into atomic and solid state science and permits accurate measurement of energy and relativistic atomic physics processes, below 1- μm accuracy or down to 1 ppm in energy.

1 | INTRODUCTION

The invention and development of the multiwire gas proportional counters (MWPCs) in 1968^[1-3] have led to the widespread use of these types of detectors across numerous fields. Of note are the investigation and discovery of new fundamental particles,^[4,5] which have led to several Nobel Prizes. MWPCs have also been successfully implemented in astrophysics,^[6] X-ray spectroscopy,^[7] and protein crystallography.^[8]

Improvements on the original design of MWPCs have been achieved through better understanding of both theory and experiment. Theoretical modelling of electrostatic effects inside the chamber^[9] and induced charge on the wires^[10] have led to a greater understanding of electronic processes, paving the way for improvements in the geometry and design of these detectors. A deeper understanding of the ionisation processes due to X-ray absorption inside the chamber from experiment has helped determine optimum operating conditions and improved resolution.^[11-13] Furthermore, the backgammon

cathode board geometry has led to an increase in spatial resolution in two-dimensional (2D) position sensitive detectors.^[14]

The technology was developed further at National Bureau of Standards to a useful size of 38 mm.^[15,16] This backgammon technology has developed with improved resolution and linearity, as well as driving ideas in detector physics worldwide.^[17-19] More recently, the position resolution of MWPCs have been shown to be comparable with charge-coupled devices (CCDs) when used in similar experimental conditions.^[20]

CCDs can have significantly better spatial pixel resolution due to the binary pixel size of, for example, 20 μm ; however, they are highly damage-sensitive,^[21,22] highly non-linear, and only operating over quite modest dynamic ranges for flux. Also, there is a challenge for single-photon-counting or event-mode operation at normal fluxes and poor real-time energy discrimination.^[23,24] After some time, the typical damage features require complex algorithms and beam-time for in situ calibra-

tion and mapping^[23,24] or replacement. Solid state detectors (germanium- and lithium-drifted silicon detectors), now segmented, have much higher energy resolution, relatively robust, and decent linearity of flux ranges but quite poor spatial resolution (pixel size often several mm). Conversely, beautiful new solid state detector technologies in these areas include the Maia detectors (CSIRO),^[25] the Pilatus detectors (PSI),^[26,27] and the Eiger detectors (PSI),^[28] with typical pixel sizes of 172 or 75 μm . These have been proven to have beam damage-resistance to a high level, with exceptional dynamic range or linearity in flux and reasonable spatial resolution. Sometimes, the cost towards several \$100,000 is significant in comparison with a backgammon detector that can be fabricated in the laboratory at a small fraction of this cost. The choice of detector will always depend on the purpose and application, and the solid state detectors can achieve high spatial resolution and relatively poor linearity (CCDs) or low spatial resolution and extremely high linearity (e.g., Pilatus, Si(Li)).

Backgammon detectors have advantages of compactness, price, and portability, together with good spatial resolution and excellent linearity. Perhaps, more particularly, backgammon technology is ideal for soft X-ray spectroscopy and even towards in-vacuum technology, for example, below 5–8 keV, where solid state detectors have low efficiency due to the windows, dead-layer, and gold contacts. The capacity to change the gas and gas pressure is a major advantage at these low energies where the absorption coefficient is increasing rapidly. However, one key challenge in earlier technology has been the flux limitation, particularly because of the charge or time-division and the arrival time of photons. We describe how this has now been improved dramatically by gating, data collection, and software processing, so that these detectors are ideally suited to many applications

including high-accuracy experimental tests of quantum electrodynamics, relativistic atomic and solid state physics, and crystallography.

2 | EXPERIMENT AND KEY CHARACTERISTICS

The operation of the University of Melbourne (UM) backgammon detector (Figure 1) relies on three main components: the anode wire, the ionising gas that fills the detector, and the backgammon cathode board. As X-rays pass through the gas, atoms of the gas are ionised, and an electron avalanche is created along with ionised atoms. The potential difference accelerates the positive gas ions towards the anode wire, with electrons accelerated towards the cathode board producing a current. The principle of resistive charge division is used to determine the position of the avalanche along the anode wire, whereas the avalanche position on the backgammon cathode board is determined by capacitive charge division on the segmented detector. A diagram of the cathode board and anode wire along side one another is shown in Figure 2. Figure 3 shows a photograph of the anode wire and cathode board. The sawtooth shape of the cathode board gives the detector its name. The ionising gas in the detector for these experiments was P10 (90% argon and 10% methane) at a voltage of 2,100 V and pressure of approximately 1,060 Torr (slightly above atmospheric pressure). Investigations have been made at a range of pressures and voltages and also with xenon–methane, which is preferable for high energy detection. For very low photon energy, nitrogen gas is useful for a high detector quantum efficiency.

Technical details of the UM backgammon detector electronics and processing are in Appendix A. Appendix B provides details on cathode board and anode wire signal processing and calibration.

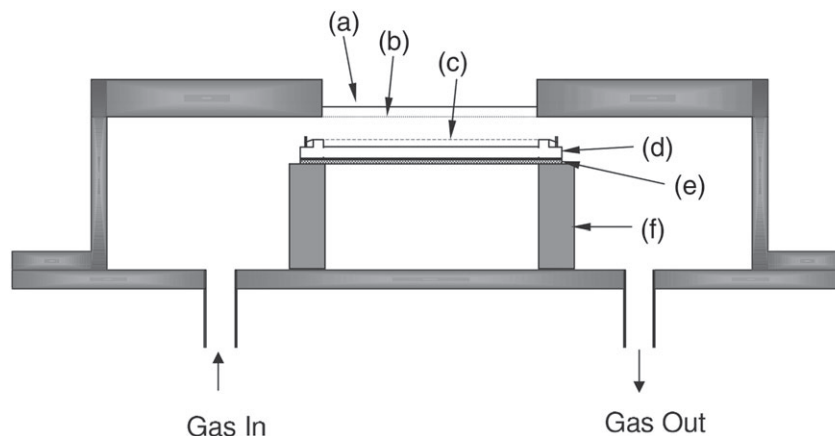


FIGURE 1 Cross-section of the internal components of the University of Melbourne backgammon detector. (a) The beryllium window. (b) Nickel mesh ground plane. (c) Platinum anode wire plane. (d) Anode wire Macor frame. (e) Cathode board. (f) Macor support structure

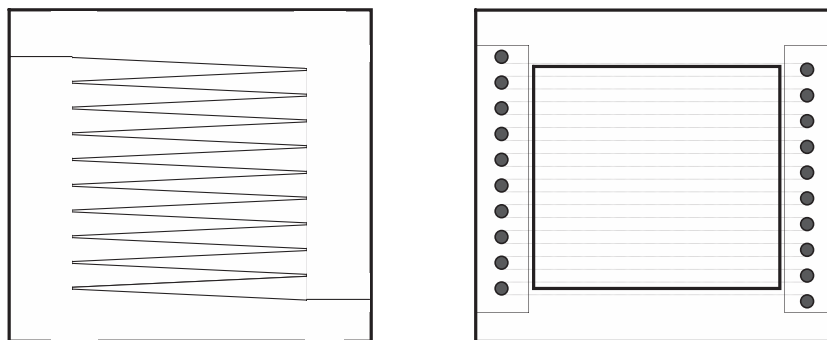


FIGURE 2 The left panel shows the segmented cathode board, separated by a 100 μm wide channel. The anode wire, shown on the right, is wrapped around gold-coated pins mounted to the Macor frame

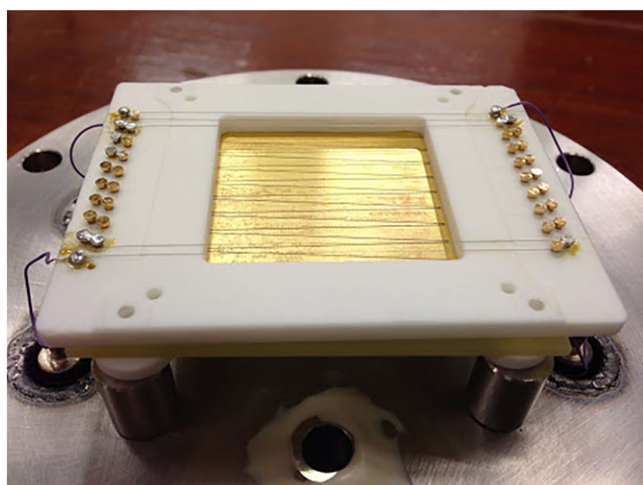


FIGURE 3 The cathode board and anode wire. The anode wire has been only partially strung so that the cathode board's backgammon shape can be seen. The gold-coated pins suspending the wire are shown, as well as the four output wires

The X-ray optics group at the UM have improved the backgammon MWPCs design over the last decades. The identification of systematics thought to be inherent to these detectors has led to a reduction in image distortions and a dramatic improvement in resolution.^[20] Improvements to the electronics of the backgammon detector have resulted in improved acquisition efficiency, diagnostic capability, and correction time.^[29,30] Simulation of non-linear effects have led to a 20% increase in the linear active region and an increased photon detection efficiency of 326%.^[31] In 2010, charge cloud modelling by Payne *et al.* was used to improve linearity.^[32] Event-mode data collection is now normal. This paper highlights the application, advantages, and utility of the most recent UM backgammon detector. The UM backgammon detector has been tested in terms of flux linearity, spatial linearity, and spatial resolution.

2.1 | Flux linearity

Characteristic X-ray radiation was generated by a MAC Science SRA M18XH1 water cooled rotating anode source. A 10 mA current was passed through a tungsten filament producing a stream of electrons incident on a Cu anode. X-rays exit the rotating anode through a 1.0 mm slit and into a collimator. The collimator consisted of a 244 ± 3 mm length lead pipe with 1.0 mm slit at the end. Once collimated, the beam was diffracted using a monolithic Si(111) channel-cut crystal (Figure 4). After being dispersed by the monochromator, the spectrum was attenuated with aluminium foils and projected onto the beryllium window of the UM backgammon detector (Figure 5). Lead panels shielded the detector face from scattered X-rays. For each attenuating thickness, the number of X-ray events detected over 10 s was recorded, and the count rate was determined. Thirteen thicknesses were examined ranging from 16 to 192 foils with 12 μm per foil.

The count rate was modelled assuming that the detector count rate responds linearly to X-ray intensity and that the X-ray beam was composed of two components: the Cu $K\alpha$ spectrum and a first-order harmonic component. The count rate in Hertz, I , is given as a function of the

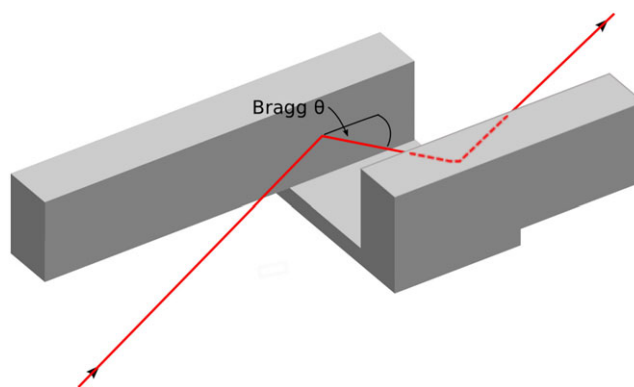


FIGURE 4 The Si(111) double bounce monochromator. The Bragg angle and the X-ray beam path are shown

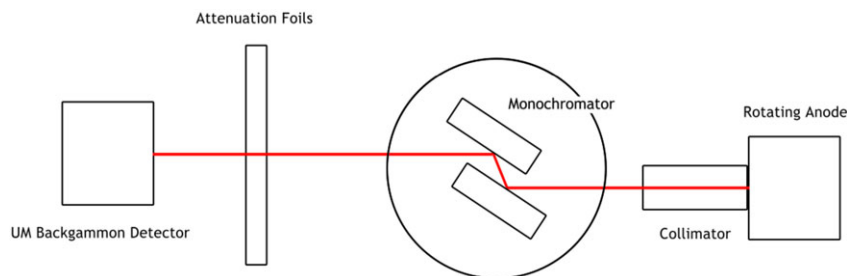


FIGURE 5 Diagram of the rotating anode experimental set-up. The rotating anode, collimator, monochromator, aluminium attenuation foil, and University of Melbourne backgammon detector are represented. The X-ray beam is collimated with 1 mm slits at each end of the collimator

attenuation thickness, measured as the number of 12 μm foils, n : $I = I_0(1 - h_f)e^{-\mu_1 t n} + I_0 h_f e^{-\mu_2 t n}$. I_0 is the incident count rate, the X-ray intensity times the detector efficiency; t is the thickness of the Al foils used; h_f is the fraction of the incident count rate due to the harmonic (higher energy) component of the beam. μ_1 and μ_2 are the linear attenuation coefficients of Al for the energy of Cu $K\alpha$, 8.04 keV and its first harmonic respectively for 16.08 keV. Values for $[\frac{\mu}{\rho}]_{1,2,3}$ are 48.411, 6.23, 1.99 cm^2/g .^[33] Hence, values $\mu_1 = [\frac{\mu}{\rho}]_1 \rho$, μ_2 and μ_3 for aluminium foils are 130.43, 16.79, and 5.36 cm^{-1} . The experimental data agree perfectly with the coefficients for μ_1 for the initial slope and with μ_2 for the higher harmonic, within 3–6%, confirming that the higher harmonic is definitively not from the 333 reflection but from the 222 reflection. It is in fact impossible to have the expected normally dominant third-order radiation (second harmonic) because the accelerating voltage is only 20 keV. We observe the direct attenuation of the beam with foil thickness with the attenuation coefficient exactly that of the forbidden second-order Si 222 reflection. This reflection is forbidden, that is, suppressed—it is non-zero due to the silicon bonding, as discussed in the International Tables for Crystallography Volume C.^[34] The intensity of the first harmonic (222) compared with the fundamental (111) can be obtained through the structure factors of Si 111 and 222: $(F_{222}/F_{111})^2 = \left(\frac{1.85 \pm 0.85}{59.87 \pm 0.46}\right)^2 \approx (0.1 \rightarrow 0.2)\%$.^[35]

Fitting the model to the data gives $\chi_r^2 = 1.3$ and plausible values for all parameters (Figure 6, Table 1). A good χ_r^2 indicates that the count rate is linear from 7 Hz up to at least 17 kHz and that the X-rays incident on the detector are composed of a Cu $K\alpha$ component and a higher energy component, from second-order Bragg diffraction. We also obtain the dark current to be 4 ± 1 Hz.

The fitted effective harmonic percentage represents the product of the overall detector efficiency and optic losses compared with that of the fundamental (8.04 keV) energy, multiplied by the actual harmonic percentage. This has been discussed elsewhere^[36]; note that the air absorption is

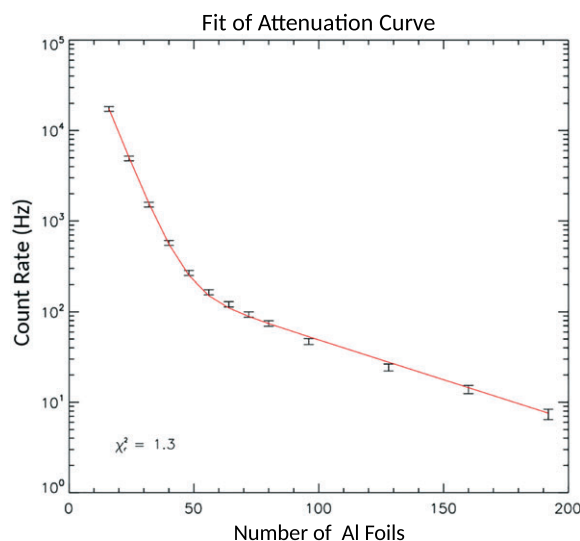


FIGURE 6 Flux linearity across four decades. This log-linear plot of attenuation shows a clear signature of two energy components attenuated by the foil thicknesses, with each foil thickness $\approx 12 \mu\text{m}$. The first straight section reflects the higher attenuation coefficient component (Cu $K\alpha$), whereas the second reflects the lower attenuation coefficient component—the higher energy first harmonic component

TABLE 1 Fitted parameters with uncertainties for Equation C1 for count rate versus thickness

Parameter	Fitted value	SD σ
I_0	213 kHz	21 kHz
t	12.07 μm	0.29 μm
h_f	0.175%	0.011%

Note. t represents the thickness per foil, consistent with previous measurements.

negligible so that the differential efficiency is dominated by the source, detector, and window components. The amplitude of the spectral intensity will vary from first-order to second-order. For a typical fixed anode source, the peak amplitude is stronger for the characteristic $K\alpha$ radiation than for the bremsstrahlung first harmonic; for a

synchrotron source, the peak source ratio might be within a factor of two; for a typical laboratory X-ray source, such as ours, the source ratio is strongly affected by the takeoff angle, self-absorption, and optical bandpass. The detector efficiency is also critically dependent upon the dead region common in all (backgammon) detectors. We have observed the 222 reflection in similar laboratory experiments with alternate detectors, so that the fitted *effective percentage* of 0.175% is quite reasonable.

2.2 | Spatial linearity

Non-linearities in the spatial response in the energy dispersive direction in an X-ray detector lead to systematic errors in the energy calibration of the spectrometer system and measurement. The backgammon detector type has a great advantage in this respect over large pixel-based detectors because the spatial signal is an analogue so that the linearity does not have a binary minimum spatial extent. A spatial calibration map for the detector was developed to map the raw output of the detector to a physical length scale, in the cathode board axis (Appendix C).

The *maximum fractional non-linearity* is defined as the maximum residual between the detector output, x , and physical length, L , at which the event took place, divided by the total length of the active region of the detector. The maximum fractional non-linearity of our detector was found to be $0.016 \text{ mm} / 22 \text{ mm} = 0.073\%$. This is a significant improvement on the previous best backgammon designs that report a maximum fractional non-linearity of 0.2%.^[29] For comparison, the detector used in the current best X-ray emission spectra experiment has a pixel size of $172 \mu\text{m}$ giving an average spatial non-linearity of $86 \mu\text{m}$, much larger than our maximum spatial non-linearity of $16 \mu\text{m}$. The maximum fraction non-linearity is the maximum extreme outlier for a single channel and is not representative of a typical uncertainty in the detector cathode position response. This overestimate of the extreme non-linearity can be dominated by statistical outliers, generally towards the edge of the detector.

Non-linearity can also be quantified by looking at the *fractional linearity uncertainty* in the fitted parameters over the linear relation, the gradient, and the offset. This measure gives an indication that, subject to noise, a broad feature can be resolved to high accuracy.

In our case, the effective non-linearity is perhaps best defined by the *regional non-linearity*, defined as the average deviation of the detected centroid from the linear fit. This measure represents the typical error of a single channel position determination, rather than the most extreme point-defect or statistical error. From Appendix C, this is of order $1 \mu\text{m}$ across the full range of the detector,

corresponding to an energy accuracy of order 2 ppm or less for Cu $K\alpha$. The overall accuracy of an experiment does not only depend on the detector used. The final accuracy, in parts per million, should account for all types of uncertainties and the parts per million quoted here is only one such systematic. However, the detector non-linearity will always contribute to this total uncertainty and is therefore an important specification of the UM backgammon detector.

3 | EXPERIMENT: RELATIVISTIC ATOMIC PHYSICS OF CHARACTERISTIC RADIATION

The backgammon type MWPCs developed at the UM have been successfully used in experiments including tests of quantum electrodynamics (QED) and high accuracy measurement of X-ray spectra.^[7,37,38] We present three new studies to illustrate the characteristics and utility.

The UM backgammon detector recorded the X-ray spectra of chromium and titanium from a Johann-type curved crystal X-ray spectrometer, operating at a near vacuum pressure, less than 10^{-7} Torr. The characteristic X-ray radiation was generated using a fluorescence source, being a 20 keV electron gun and a metal target (Figure 7). The electrons incident on the metal target create the corresponding $K\alpha$ radiation.

The radiation is diffracted using a Ge(220) curved crystal monochromator and projected onto the detector face at the end of the detector arm. The electron gun beam was normal to both the metal target-to-crystal and crystal-to-detector X-ray beams. The detector was placed 1.5 m from the crystal monochromator, each positioned on the rowland circle to ensure the focusing and maximum intensity of X-ray photons (Figure 8). Figure 8 illustrates the target element, the 2θ angle of the detector arm, and the adjustable wedge that can alter bandpass, instrumental broadening (vignetting), and other spectral systematics.

The detector arm angle was measured by 2 gravity-referenced clinometers, with voltage as the raw output. These were placed at the base and top of the detector arm. Before the experiment, each had been calibrated against a Heidenhain ROD 800 interferometric encoder using a Huber 410 goniometer. A Huber SMC 9000 motor controller controlled the angular motion. For each element, three runs were performed, with runtimes of roughly 20 min giving the number of counts at the peak of the spectra in the order of 10^4 . For each run, the detector arm was rotated slightly, so the spectra would be incident on different positions along the detector face. This defined clinometer

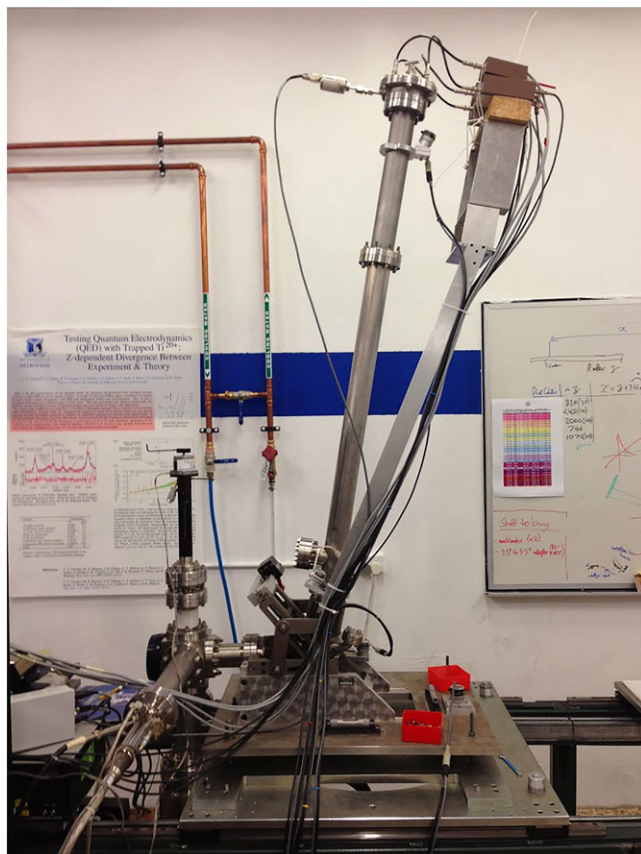


FIGURE 7 Fluorescent source experimental set-up, used to obtain spectra of Cr and Ti. The UM backgammon detector can be seen at the end of the detector arm, as well as the electron gun normal to the target-crystal beam running across the page

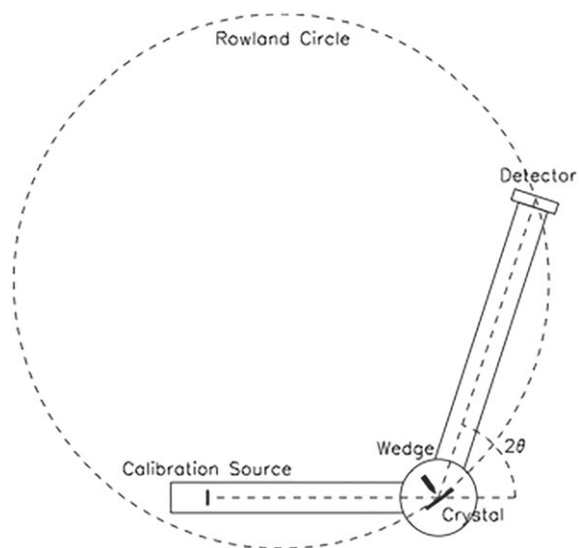


FIGURE 8 Schematic diagram of the fluorescent source experimental set-up, used to obtain the spectra of Cr and Ti

calibration and the 2θ angle. The detector outputs 2D histograms showing the events measured across the detector face (Appendix A).

The 2D histograms show the distribution of the photon–gas interaction on the detector face. Values in each x -channel were summed to yield one-dimensional spectra with counts as function of x -channel. The monochromator relates x to energy. Each spectra were summed after calibration using a calibration map from a slit-illuminated source (Appendix C).

4 | PROFILE ANALYSIS AND QUALITY OF SPECTRA

The best measurement available of the chromium $K\alpha$ spectrum^[39] was characterised by fitting the sum of six Lorentzian functions to the data after a deconvolution.

Two characterisations of the titanium $K\alpha$ spectrum are presented.^[37] Each has been found by fitting the sum of six Voigt functions, with a common Gaussian broadening term, to data previously published.^[40,41] These parameterisations are considered the best thus far.

The quality of the fluorescent source and UM backgammon detector was tested by measuring chromium and titanium data collected. Most large-pixel detectors cannot be mounted on the detector arm in this vertical orientation of the spectrometer because of their weight and bulk. A Levenberg–Marquardt fitting procedure fitted Voigt profile characterisations following other works.^[37,39] The energy scale was calibrated by the energy difference between $K\alpha_{11}$ and $K\alpha_{21}$. Common Gaussian and Lorentzian widths capture instrumental broadening.

Figures 9 and 10 show our data parameterised by these state-of-the-art measurement standards. Fitting the Cr spectrum yielded $\chi_r^2 = 2.20$. Fitting the Ti spectrum yielded $\chi_r^2 = 1.67$. Both indicate excellent resolution, profile consistency, and linearity. Both spectra show two well-separated peaks, no signs of non-linearities, low noise, and residuals typical of X-ray spectra. Any instrumental broadening has been modelled using Voigts rather than Lorentzians. Even with our modest broadening, our Cr $K\alpha$ spectrum compares quite well with figure 1a from Hölzer et al.^[39] A low χ_r^2 indicates that our data are consistent with spectra obtained using the best solid state detectors available. Both indicate some correlated noise in the residual, which is also characteristic of the earlier world best characterisations. This high level probe of X-ray structure, of relativistic atomic physics, and of calibration standards and methodology is important for standard X-ray sources and advanced experiments. This demonstrates clearly the capability of the UM backgammon detector to measure characteristic and general X-ray spectra comparable with the state-of-the-art for any detection system.

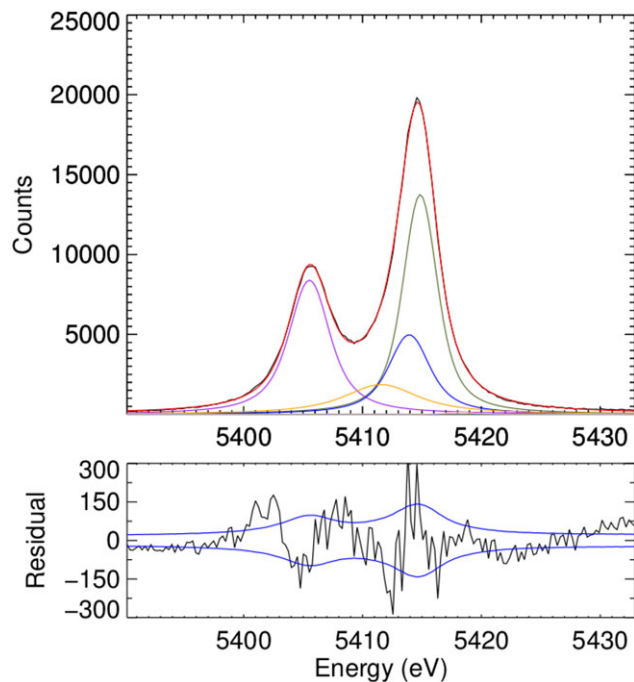


FIGURE 9 High-resolution spectral profile of Cr $K\alpha$ obtained with the UM Backgammon detector, with excellent fit to the current best characterisation of Cr $K\alpha$ ($\chi_r^2 = 2.20$);^[37,39] The profile, above, indicates the component peaks from the characterisation. The residuals in black, below, are compared with the 1-standard error envelope in blue. Some correlated residual noise is observable, as found in the data sets of the reference characterisations with different source and detector optics

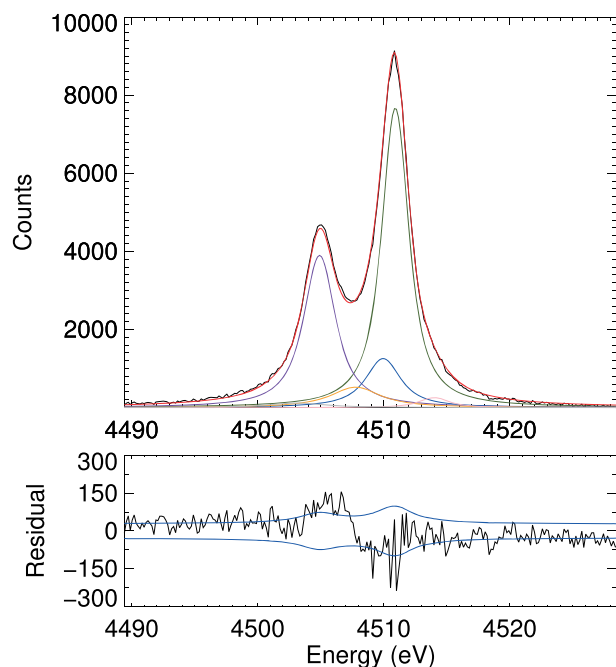


FIGURE 10 High-resolution spectral profile of titanium $K\alpha$ obtained with the UM Backgammon detector, with excellent fit to the current best characterisation ($\chi_r^2 = 1.67$)^[37]

The resolution of a detector, when used in X-ray spectroscopy, allows the determination of individual components in the spectra. The total broadening present in our data can be quantified by looking at the common broadening of the fits. This total broadening is made up two parts: the instrument function point spread function (PSF) inherent to the spectrometer itself and the broadening (PSF) due to the detector resolution. The instrumental broadening function or PSF of the spectrometer was estimated using dynamic diffraction modelling *Mosplate*.^[42–44] The detector broadening (PSF) was a consistent residual after the removal of the instrumental broadening function in quadrature, of $240 \mu\text{m}$ with an estimated uncertainty of $\pm 20 \mu\text{m}$. This is a significant improvement on the resolution of $330 \mu\text{m} \pm 30 \mu\text{m}$ of earlier designs.^[29]

5 | EXPERIMENT: COPPER $K\alpha$ AND ROTATING ANODE SPECTRA

The UM backgammon detector also investigated the X-ray spectrum of copper metal in a qualitatively different experimental set-up using the UM rotating anode. Characteristic X-ray radiation was generated by a MACScience SRA M18XH1 water cooled rotating anode source. The Si(111) crystal has a lattice, $d = 3.1356 \text{ \AA}$. This gives a Bragg angle for $K\alpha_1$ of 14.219° and 14.258° for $K\alpha_2$. These correspond to energies of 8047.78 and 8027.83 eV, respectively. The angle between the X-ray and the double bounce Si(111) monochromator normal (Figure 4) was set between these angles. After being dispersed by the monochromator, the spectrum was attenuated with aluminium and projected onto the beryllium window of the UM backgammon detector. Lead panels shielded the detector from scattered X-rays (Figure 5).

The detector was set to a voltage of $2,100$ V, using P10 (90% argon and 10% methane) as the ionising gas. Multiple profiles of the Cu $K\alpha$ spectrum were taken with exposure times of $7,200$ s. The rotating anode voltage was set to 20 kV, where the $K\alpha$ spectrum has been shown to be stable.^[45] A highly attenuated background exposure was also taken, only allowing residual high energy X-rays to reach the detector face, to separate fundamental and higher order scattered radiation (Appendix D). Table 2 summarises the measured profiles.

The Cu spectrum was obtained from the raw data in the same manner as the Cr and Ti spectra. Figure 11 shows the well-resolved Cu spectrum. The amount of instrumental broadening in X-ray spectra is different for each experiment, depending upon the experimental geometry, spectrometer instrument function and divergence. To compare our data to the literature spectra, the broadening

TABLE 2 Experimental details of the Cu $K\alpha$ measurements

	No. of foils	Exposure time	Current	Total Counts	Frequency
		(s)	(mA)		(Hz)
File 1	32	7,200	14	6,553,428	910.2
File 2	24	7,200	10	8,339,156	1,158.2
File 3	24	7,200	10	8,343,119	1,158.8
Background	104	1,200	200	1,506,841	1,255.7

Note. The frequency column shows the rate at which X-ray events were counted.

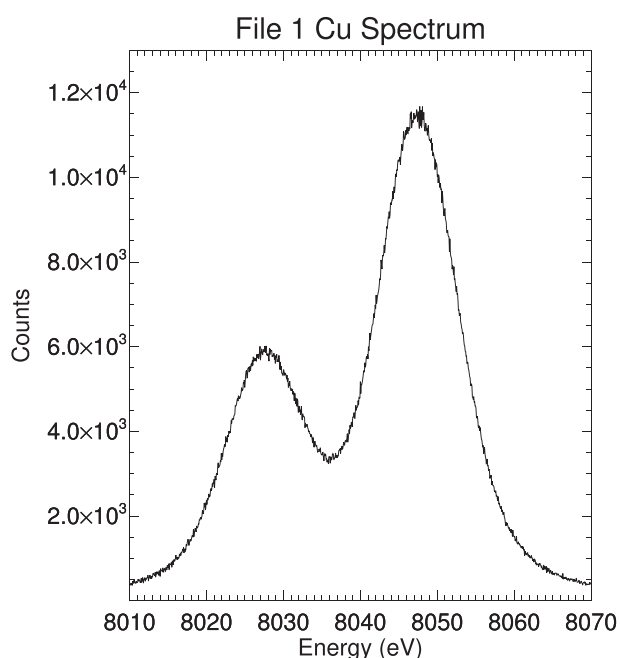


FIGURE 11 The good resolution spectral profile of the File 1 Cu $K\alpha$ data, obtained from the rotating anode and University of Melbourne backgammon detector. The $K\alpha_1$ and $K\alpha_2$ peaks are well separated

is removed using a deconvolution.^[39] This assumes that the broadening is uniform across the spectrum. For the Cu file 1 data, shown in Figure 12, the amount of Gaussian and Lorentzian broadening removed was 9.243 and 2.852 eV, respectively. The quality of the spectra again demonstrates the UM backgammon detector capability.

The deconvolved Cu spectrum (Figure 12) compares well with Cu X-ray spectra from the literature^[46]; their Figure 4 displays the deconvolved Cu $K\alpha$ spectra. More recently, the Cu $K\alpha$ has been measured using a Pilatus 100 K solid state detector.^[47] Our results (Figure 12) also match well with those in Figure 19 of their publication. This detector technology is able to measure X-ray spectra consistent with the current best technologies and long-lasting literature standards. In particular, the analogue measurement enables a continuous spectral representation with an accuracy to below 1 ppm in energy (0.0001%).

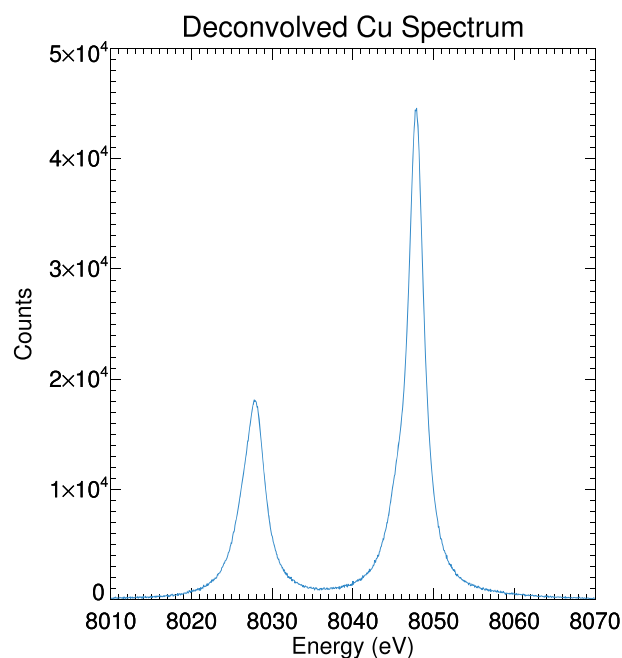


FIGURE 12 The deconvolved spectrum compares extremely well to the published literature^[46,47]

6 | DISCUSSION

QED is the current best description of the interaction between electromagnetic radiation and electric charge. Discrepancies between experimentally measured energies of the Lamb shift and those predicted by theory are key in many tests of QED. One probe is to look at hydrogen-like and helium-like medium Z ions, as here the scaling of corrections allow feasible precision and low nuclear effects. These tests require detectors capable of highly accurate energy determination across a range of fluxes. The UM backgammon detector's high degree of spatial linearity makes it capable of measuring energies to a few parts per million, as well as being highly linear in terms of count rate. Coupled with a satisfactory resolution the UM backgammon detector is well suited to such QED tests and high accuracy X-ray spectroscopy experiments.

A maximum fractional non-linearity of 0.073% amounts to a significant improvement on the best previous designs,

TABLE 3 Widths and energies with standard deviation uncertainties and χ_r^2 of fits using the current literature standards with instrumental broadening indicated from the source, optic, spectrometer, and detector configuration

	Z	$K\alpha_{11}$ Energy (eV)	χ_r^2	Gaussian width (eV)	Lorentzian width (eV)
Titanium	22	4510.926 ± 0.014	1.54	1.018 ± 0.025	0.786 ± 0.025
Chromium	24	5414.874 ± 0.002	2.20	2.049 ± 0.015	0.782 ± 0.021
Copper	29	8047.837 ± 0.002	2.08	9.243 ± 0.018	2.852 ± 0.020

Note. Results for Cu are for File 1 data taken with the rotating anode source. Low χ_r^2 across different experimental geometries and energies highlight the detectors utility.

which demonstrate a maximum fractional non-linearity of 0.2%.^[16,29] The regional non-linearity implies accuracies to 1 μm and below and clearly permits measurement accuracies to sub- μm and of order 1 ppm. The fractional non-linearity of our detector, regardless of which measure you consider, is significantly smaller than that achievable by the best solid state available. A pixel size of 172 and 75 μm , for the Pilatus and Eigar detectors, respectively, means that non-linearities of 86 and 37.5 μm are quite significant for high-accuracy measurement.

A sophisticated data acquisition system for our detector enable single photon counting and efficiencies over a range of flux, 1 Hz–50 kHz (see Appendix A). The UM backgammon detector has been shown to be linear in intensity up to at least 17 kHz. This is especially significant when comparing with CCD non-linearities at high count rates or over intensity ranges above two decadal ranges.

The Cr and Ti data, taken with the fluorescence source, have been fitted following other works^[37,39] with excellent χ_r^2 indicating that data obtained with the UM backgammon detector are consistent with that published in the literature. Table 3 indicates that the broadening present is not significant for the Ti and Cr spectra.

The Cu spectrum, measured using the rotating anode laboratory source, was also fitted using one of the current best parameterisations available.^[39] The Cu spectra (Figure 11) contain a higher instrumental broadening from source and monochromator compared with those taken with the fluorescence source (Figures 9 and 10), and fits well in this alternate experimental set-up. A low χ_r^2 demonstrates the robustness of the detector over a range of energies and experimental geometries.

7 | CONCLUSION

Experiments striving to probe phenomena at increasing levels of sensitivity rely on advanced detectors. The collected data for the $K\alpha$ splitting of copper, chromium, and titanium, and the capacity to make critical tests of QED, demonstrate that the UM backgammon detector is capable of recording highly accurate X-ray spectra over a wide

range of energies. The collected data are comparable, and superior in several respects, to those taken with CCDs that have sometimes been preferable in certain fields of experimental physics.

The regional non-linearity of 1 μm allows the detection of photons to be readily determined down to 1–2 ppm in energy, an improvement on similarly designed MWPC detector devices. Furthermore, the ability to alter the gas that fills the detector and the ionisation mechanism ensures that a wide range of photon energies can be resolved at a similar resolution. Also significant is the quality fitting of data using the best available parameterisations. Low χ_r^2 show that the quality compared with what has previously been published despite different experimental conditions, set-ups and detector geometry. After the removal of the common broadening, the spectra recorded in the described experiments match well with those previously published. The detector allows previous experiments to be used as calibrations for future experiments, with the raw calibration of incident photon position on the detector face and improvements to the data analysis and processing. The popularity of MWPCs in X-ray spectrometry and other areas of measurement science remains very strong.

ACKNOWLEDGEMENTS

We acknowledge A. T. Payne for his part in the development of the backgammon detector technology and of the data acquisition. We acknowledge the group of X-ray Optical and Synchrotron Science at the School of Physics.

ORCID

Christopher T. Chantler  <https://orcid.org/0000-0001-6608-0048>

REFERENCES

- [1] G. Charpak, R. Bouclier, T. Bressani, J. Favier, Č. Zupančič, *Nucl. Instrum. Methods* **1968**, 62(3), 262.
- [2] G. Charpak, D. Rahm, H. Steiner, *Nucl. Instrum. Methods* **1970**, 80, 13.

- [3] G. Charpak, F. Sauli, *Nucl. Instrum. Methods* **1973**, *113*, 381.
- [4] B. Richter, *Rev. Mod. Phys.* **1977**, *49*(2), 251.
- [5] C. Rubbia, *Rev. Mod. Phys.* **1985**, *57*(3), 699.
- [6] L. Horton, J. Ulrichs, M. Winn, *Nucl. Inst. Methods Phys. Res. A* **1992**, *325*(1993), 326.
- [7] C. T. Chantler, D. Paterson, L. T. Hudson, F. G. Serpa, J. D. Gillaspay, E. Taka, *Phys. Rev. A* **2000**, *62*, 1.
- [8] F. Ortuno-Prados, A. Bazzano, A. Berry, C. Budtz-Jorgensen, C. Hall, W. Helsby, R. Lewis, B. Parker, P. Ubertini, *Nucl. Inst. Methods Phys. Res. A* **1999**, *420*, 446.
- [9] G. A. Erskine, *Nucl. Instrum. Methods* **1972**, *105*, 565.
- [10] G. A. Erskine, *Nucl. Instrum. Methods* **1982**, *198*, 325.
- [11] G. C. Smith, J. Fischer, V. Radeka, *IEEE Trans. Nucl. Sci.* **1984**, *NS-31*(1), 111.
- [12] J. Fischer, V. Radeka, G. C. Smith, *Nucl. Inst. Methods Phys. Res. A* **1986**, *252*, 239.
- [13] J. Fischer, V. Radeka, G. C. Smith, *IEEE Trans. Nucl. Sci.* **1986**, *33*(1), 257.
- [14] R. Allemand, G. Thomas, *Nucl. Instrum. Methods* **1976**, *137*(1), 141.
- [15] B. P. Duval, J. Barth, R. D. Deslattes, A. Henins, G. G. Luther, *Nucl. Instrum. Methods Phys. Res.* **1984**, *222*, 274.
- [16] G. G. Luther, P. L. Cowan, A. Henins, S. Brennan, *Nucl. Inst. Methods Phys. Res. A* **1986**, *246*(1), 537.
- [17] T. Mizogawa, M. Sato, Y. Awaya, *Nucl. Instrum. Methods Phys. Res., Sect. A* **1995**, *366*(1), 129.
- [18] G. Veshapidze, T. Nishide, H. Shiromaru, N. Kobayashi, T. Mizogawa, *Jpn. J. Appl. Phys.* **2002**, *41*(2R), 871.
- [19] T. Mizogawa, H. Shiromaru, M. Sato, Y. Ito, *Int. J. Mass Spectrom.* **2002**, *215*(1), 141. Detectors and the Measurement of Mass Spectra.
- [20] M. N. Kinnane, J. A. Kimpton, M. D. D. Jonge, K. Makonyi, C. T. Chantler, *Meas. Sci. Technol.* **2005**, *16*, 2280.
- [21] J. Janesick, T. Elliott, F. Pool, *IEEE Trans. Nucl. Sci.* **1989**, *36*(1), 572.
- [22] N. Bassler, *Radiat. Environ. Biophys.* **2010**, *49*(3), 373.
- [23] L. T. Hudson, J. D. Gillaspay, J. M. Pomeroy, C. I. Szabo, J. N. Tan, B. Radics, E. Takacs, C. T. Chantler, J. A. Kimpton, M. N. Kinnane, L. F. Smale, *Nucl. Inst. Methods Phys. Res. A* **2007**, *580*, 33.
- [24] L. F. Smale, C. T. Chantler, L. T. Hudson, *Nucl. Inst. Methods Phys. Res. A* **2010**, *619*, 150.
- [25] C. G. Ryan, D. P. Siddons, R. Kirkham, Z. Y. Li, M. D. de Jonge, D. J. Paterson, A. Kuczewski, D. L. Howard, P. A. Dunn, G. Falkenberg, U. Boesenberg, G. De Geronimo, L. A. Fisher, A. Halfpenny, M. J. Lintern, E. Lombi, K. A. Dyl, M. Jensen, G. F. Moorhead, J. S. Cleverley, R. M. Hough, B. Godel, S. J. Barnes, S. A. James, K. M. Spiers, M. Alfeld, G. Wellenreuther, Z. Vukmanovic, S. Borg, *Journal of Physics: Conference Series* **2014**, *499*(012002), 1.
- [26] C. Broennimann, E. F. Eikenberry, B. Henrich, R. Horisberger, G. Huelsen, E. Pohl, B. Schmitt, C. Schulze-Briese, M. Suzuki, T. Tomizaki, H. Toyokawa, A. Wagner, *J. Synchrotron Radiat.* **2006**, *13*(2), 120.
- [27] B. A. Sobott, C. Broennimann, B. Schmitt, P. Trueb, M. Schneebeli, V. Lee, D. J. Peake, S. Elbracht-Leong, A. Schubert, N. Kirby, M. J. Boland, C. T. Chantler, Z. Barnea, R. P. Rassool, *J. Synchrotron Radiat.* **2013**, *20*, 347.
- [28] R. Dinapoli, A. Bergamaschi, B. Henrich, R. Horisberger, I. Johnson, A. Mozzanica, E. Schmid, B. Schmitt, A. Schreiber, X. Shi, G. Theidel, *Nucl. Instrum. Methods Phys. Res., Sect. A* **2011**, *650*(1), 79.
- [29] J. A. Kimpton, M. N. Kinnane, C. T. Chantler, *Rev. Sci. Instrum.* **2006**, *77*(8), 1.
- [30] J. A. Kimpton, M. N. Kinnane, L. F. Smale, C. T. Chantler, L. T. Hudson, A. Henins, *Nucl. Inst. Methods Phys. Res. A* **2007**, *580*, 246.
- [31] A. T. Payne, J. A. Kimpton, M. N. Kinnane, C. T. Chantler, *Meas. Sci. Technol.* **2009**, *20*, 7.
- [32] A. Payne, J. A. Kimpton, L. F. Smale, C. T. Chantler, *Nucl. Inst. Methods Phys. Res. A* **2010**, *619*(1-3), 190.
- [33] C. T. Chantler, *J. Phys. Chem. Ref. Data* **1995**, *24*, 71.
- [34] U. W. Arndt, R. D. Deslattes, E. G. Kessler, P. Indelicato, E. Lindroth, D. C. Creagh, J. H. Hubbell, in *International tables for crystallography*, vol. c, (Eds: A. J. C. Wilson, E. Prince), Kluwer Academic Publishers, Dordrecht **1999**, 191.
- [35] Y. Ando, A. Ichimiya, R. Uyeda, *Acta Crystallogr. A* **1974**, *30*(4), 600.
- [36] J. L. Glover, C. T. Chantler, *X-Ray Spectrom.* **2009**, *38*, 510.
- [37] C. T. Chantler, M. N. Kinnane, C. Su, J. A. Kimpton, *Phys. Rev. A* **2006**, *73*(012508), 1.
- [38] C. T. Chantler, M. N. Kinnane, J. D. Gillaspay, L. T. Hudson, A. T. Payne, L. F. Smale, A. Henins, J. M. Pomeroy, J. N. Tan, J. A. Kimpton, E. Takacs, K. Makonyi, *Phys. Rev. Lett.* **2012**, *109*(15), 1.
- [39] G. Hölzer, M. Fritsch, M. Deutsch, J. Härtwig, E. Förster, *Phys. Rev. A* **1997**, *56*(6), 4554.
- [40] J. Kawai, T. Konishi, A. Shimohara, Y. Gohshi, *Spectrochim. Acta B At. Spectrosc.* **1994**, *49*(7), 725.
- [41] D. F. Anagnostopoulos, D. Gotta, P. Indelicato, L. M. Simons, *Phys. Rev. Lett.* **2003**, *91*(24), 12.
- [42] C. T. Chantler, *J. Appl. Crystallogr.* **1992**, *25*(pt 6), 674.
- [43] C. T. Chantler, *J. Appl. Crystallogr.* **1992**, *25*(pt 6), 694.
- [44] C. T. Chantler, R. D. Deslattes, *Rev. Sci. Instrum.* **1995**, *66*(11), 5123.
- [45] A. J. Illig, C. T. Chantler, A. T. Payne, *J. Phys. B: At., Mol. Opt. Phys.* **2013**, *46*(23), 235001.
- [46] M. Deutsch, G. Holzer, J. Hartwig, J. Wolf, M. Fritsch, E. Forster, *Phys. Rev. A* **1995**, *51*(1), 283.
- [47] M. H. Mendenhall, A. Henins, L. T. Hudson, C. I. Szabo, D. Windover, J. P. Cline, *J. Phys. B: At., Mol. Opt. Phys.* **2017**, *50*(115004), 1.

How to cite this article: Melia HA, Dean JW, Smale LF, Illig AJ, Chantler CT. Count-rate, linearity, and performance of new backgammon detector technology. *X-Ray Spectrometry*. 2019;48:218–231. <https://doi.org/10.1002/xrs.3024>

APPENDIX A: ELECTRONICS AND PROCESSING

The University of Melbourne (UM) backgammon detector relies on a sophisticated data acquisition system specifically developed for the detector and its use as part of our Johann-type curved crystal X-ray spectrometer. The design allows single photon counting over a wide range of count rates.^[30]

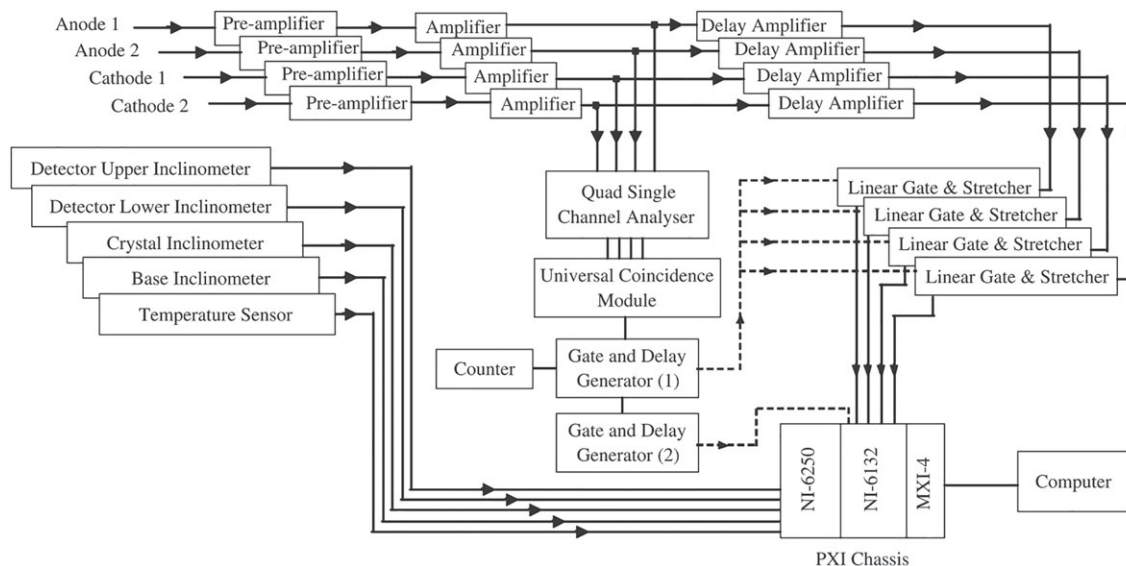


FIGURE A1 Schematic of the data acquisition system: detector signal processing electronics, inclinometers, temperature sensor, and PXI chassis^[30]

The data acquisition system used in the UM backgammon detector takes the four outputs of the detector: two from the cathode and two from the anode. The four signals are integrated over four independent charge sensitive pre-amplifiers and balanced by independent shaping amplifiers. A universal coincidence module is used to determine signals from the same photon-gas event by matching pulses recorded within $0.2 \mu\text{s}$. Two gate and delay generators are used: the first to enable the passing of the sampled and held, shaped, and stretched data and the second enabling the acquisition. A PXI chassis with a 3 MHz four-channel simultaneous-sampling 145 bit digitiser is used to digitise each analogue signal. The chassis is connected to a PC running labVIEW. The PC controls the hardware, calculates and outputs the encoded detector data, and stores raw data. A schematic of the system is shown in Figure A1.

When the UM backgammon detector is used with the Johann-type curved crystal spectrometer, the data acquisition system also provides digitisation of the four inclinometers and temperature data. Importantly, this is done via a high-speed serial MXI-4 interface capable of sustained data transfer at a rate of 78 MB/s, allowing improved acquisition efficiency count rates in the 1 Hz–50 kHz range.

APPENDIX B: SIGNAL PROCESSING AND LINEARISATION

For each experiment, the data collection was performed using the electronic outputs of the UM's backgammon detector. For each photon-gas interaction, a region of the

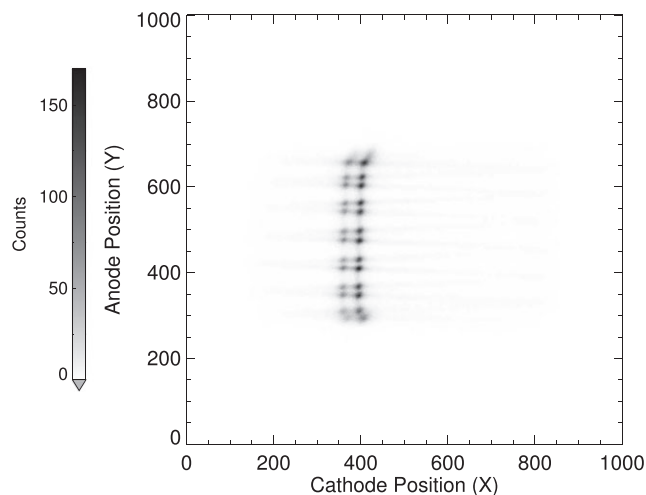


FIGURE B1 The raw, uncalibrated 2D histogram of Cr $K\alpha$, showing the photon-gas signal in the counters. These raw signals need calibration, like any detector, and illustrate wire components and near-edge field distortion. Edge or guard wire segments can be removed from analysis or corrected for as with all MWPC processing

argon gas is ionised; an electron avalanche is created and recorded by the cathode board. The ionised gas particles are similarly measured by the anode wire. This produces a voltage reading at each end of the cathode board and anode wire giving four output voltages: two voltages, A and B, from the anode wire and two, C and D, from the cathode board. The signal amplitudes are digitised and converted into a spatial position, x-y, on the detector through the equations:

$$x = \frac{C}{C+D}; \quad y = \frac{A}{A+B}. \quad (\text{B1})$$

The detector face was partitioned in each direction into 1,000 channels. Raw data could then be represented as a 2D histogram representing the number of photon–gas interactions occurring in each area of the detector. Figure B1 illustrates the raw output for Cr $K\alpha$ spectrum. The 13 distinct horizontal “rows” are representative of the 13 anode wire segments of the detector; the two separate “dots” within each wire are representative of distinct $K\alpha_1$ and $K\alpha_2$ lines. There are also additional counts along each of the anode wires due to noise and background.

The raw signal is structured at the top and bottom of the detector face. Sources of this spatial non-linearity include charge attenuation, asymmetric electric fields, and bimodal charge distribution. Although the backgammon detector has been designed to minimise these effects, the geometry of the device means that they are still present in the top and bottom wires due to non-uniform electric fields and edge effects prior to calibration, as with all similar detector types.^[20] To correct this, the data must be linearised or the end wire segments deleted or left as guard rails.

The data from the backgammon detector were linearised using a calibration map. The map was created through a calibration experiment using the rotating anode at the UM. Linearisation is needed to transform the x value, obtained from equation B1, to the *input* position - where the photon hits the detector face. This is the purpose of the calibration map. The rotating anode was used to produce a Cu $K\beta$ profile that was then collimated, passed through the

monochromator and projected onto the detector face as in the Cu $K\alpha$ experiment. The detector was mounted on a linear stage, such that when the linear stage shifted in the horizontal, the line source moved across the detector face illuminating a different vertical slice of the detector. The centre of the detector was found, and the corresponding position of the linear stage (L) was defined as 0 mm. Profiles were taken from $L = -20\text{mm}$ to $L = 20\text{mm}$. A 2D histogram was created for each physical position L with the x -axis split into 1,000 channels and the y -axis split into 500 rows. For each row, a 1D histogram was created, showing the x position that the detector measured an X-ray event hitting the detector at L . A Gaussian was fitted to the histogram for each row. The position of this Gaussian could then be used as a measure of the output position x as a response to a photon hitting the detector at a physical position L . This relationship was in general different for each row. The difference between the output x value and the associated L is a measure of the non-linearity in the x direction in that row of the detector. To remove this non-linearity, a map was created to take x to L through a fitted polynomial for each row. Polynomials of degree 2 to degree 20 were investigated. Degree 11 was found to be sufficient and stable. These 500 polynomials (one for each row) defined the calibration of detector response to an X-ray event happening at L . The result of the map is shown in Figure B2.

The images were rotated; the column was summed, and their full width at half maximum (FWHM) was recorded.

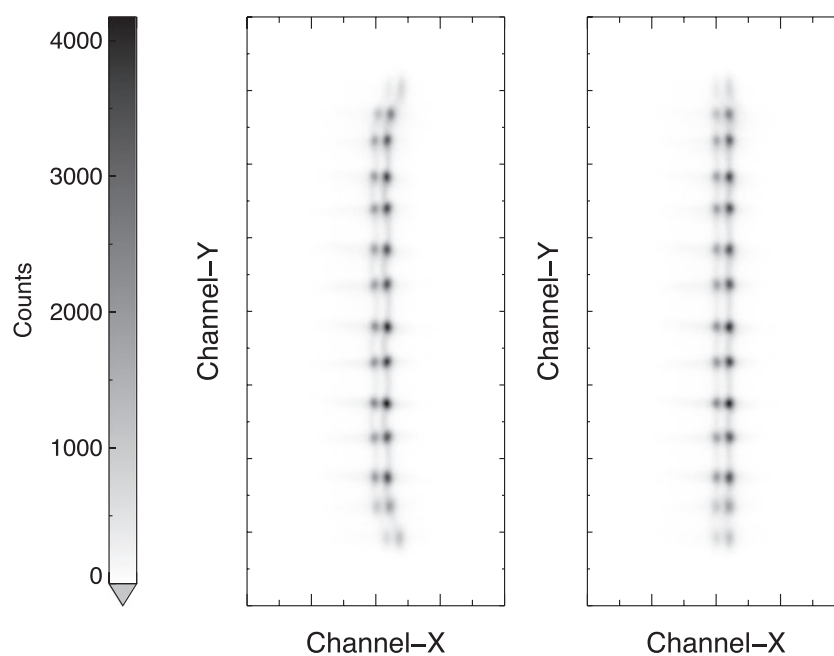


FIGURE B2 The left hand window shows the pre-processed image for the Cu data. The right hand window shows the corresponding linearised data. The “dots” show the position of the $K\alpha_1$ (right) and $K\alpha_2$ (left) peaks on the backgammon’s anode wires. Comparing the two images shows that the distortions of the field and position are, unsurprisingly, dominated by the end wires at the top and bottom of the detector

The rotation that gave the smallest FWHM was chosen for each spectrum. For the Ti and Cr data, this was found to be -1.8° . The Cu data were aligned well and required no rotation. Figure B2 shows the end-wire distortion in the horizontal direction corrected by the linearisation map of the Cu data. The end anode wires for the Ti and Cr data were removed before column summing. Similarly, the Cr and Ti images required a horizontal shifting of the odd wires. The amount of shifting was determined by minimising the FWHM of $K\alpha_1$.

APPENDIX C: LINEARITY TESTS AND DETAILS

Spatial linearity is an important feature of any detector as it enables accurate energy determination. In X-ray spectroscopy this allows the resolution of distinct energy peaks attributed to electronic transitions. Previous backgammon detector designs have quantified linearity in a number of ways. Payne et al. and Kimpton et al. both provide a thorough analysis of a linearity experiment similar to our own.^[29,31]

The non-linearity of our detector after calibration can be quantified by plotting the centre of mass of the 1D histograms, taken in the calibration experiment, against the position on the detector that the image was taken, L . To measure the centre of mass of the 1D histogram, each histogram was fitted with the sum of two Lorentzian functions plus a background constant. The centre of mass was then calculated on the fitted function above 20% of the maximum height.

A straight line was fitted to the centre of mass versus linear stage position (Equation C1). A line of best fit is used to model the relationship between the position on the detector that a Cu $K\beta$ spectrum is taken and the position that the detector measures the event. The fit is defined to a small fraction of $0.01 \mu\text{m}$ showing a good stability over the active area.

Non-linearity can also be quantified by looking at the uncertainty in the parameters of the fit, the gradient, and the offset. Payne et al. provide a fractional uncertainty in the fitted gradient of 0.019% and 0.005% in the offset, whereas Kimpton et al. report a fractional uncertainty for both fitted parameters of 0.0001%. The fractional uncertainty in our fitted parameters are 1.165% for the offset and 0.00041% for the gradient.

$$y_{fit} = (1.0018904 \pm 0.0000041) \times StagePosition + (0.002232 \pm 0.000026) \text{ mm.} \quad (\text{C1})$$

The residuals give a measure of the non-linearity of measurement after calibration. The *maximum fractional non-linearity* is defined as the maximum residual between

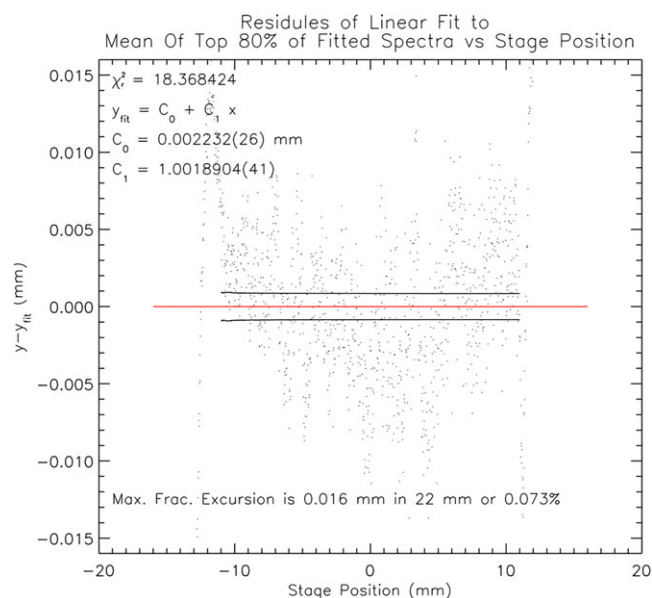


FIGURE C1 The residuals of a straight line fit of central tendency of the fitted spectra to the linear stage position are shown. The black lines are the uncertainty envelope of the central tendency

the detector output, x , and physical length, L , at which the event took place, divided by the total length of the active region of the detector. Kimpton et al.^[30] demonstrate a maximum fractional non-linearity of 0.2%. Similarly, Payne et al.^[32] provide a value of 0.345%. Our maximum is a significant improvement on both of these. The maximum residual in the 22-mm active region of our detector was $16 \mu\text{m}$, giving a fractional non-linearity value of 0.073%. All residuals within the effective active region of the detector (the middle 22 mm) were below 16 microns and almost all within 10 microns (Figure C1). This gives a quantitative value for the non-linearity, over the active region, of at most, the *maximum fractional non-linearity*, of 0.073%. For the relevant Cu $K\beta$ spectrum, used in the linearity test, 0.073% corresponds to 50 ppm in energy. Good statistics and the use of a larger bin size mean that even the worst case scenario is much more accurate than 50 ppm.

Payne et al.^[32] define the *regional differential non-linearity* as the mean of the experimental residual from the model after box-car filtering over 11 points. This measure is useful as it suppresses random statistical noise leaving a measure of the typical excursion from the detector output and the fit.

Payne et al.^[32] define the *regional non-linearity* as the average deviation of the detected centroid from the linear fit and provide this as a percentage to be 0.068%. This measure represents the typical error of a single channel position determination. Kimpton et al.^[30] estimate a regional non-linearity of 0.025%. In Figure C1, we see this to be approximately $1 \mu\text{m}$ or 0.0045%. This is a robust estimate of the error of a broad feature in a map and represents an

uncertainty for the measurement of Cu $K\alpha$ of about 2 ppm in energy.

APPENDIX D: BACKGROUND SUBTRACTION

The raw Cu data, taken with the rotating anode source, contained two components: the Cu $K\alpha$ spectrum and also the higher energy background or scattered X-rays. To isolate these, a high attenuation background exposure was

taken. This background could then be modelled in the fitting process along with the other components of the spectra, $K\alpha_{ij}$, adding one parameter to the fitting function, a scale to control the magnitude of the background present in the data. The background component was largely proportional to exposure (time \times current) and was attenuated partly by the foils, consistent with being a higher energy component.